The International Journal of Advanced Manufacturing Technology (2023) 126:5163–5178
https://doi.org/10.1007/s00170-023-11422-0

ORIGINAL ARTICLE

Analysis of self-tapping screw joints in fibre glass reinforced PEI polymer used in the automotive industry

Wilmer E. Cumbicus[1] · Manuel Estrems[1] · Miguel Arizmendi[2] · Amaya Jiménez[2]

Received: 13 December 2022 / Accepted: 6 April 2023 / Published online: 28 April 2023

Abstract

This article presents a study of the joining of polyetherimide (PEI) polymer parts reinforced with fibre glass which has great application in the automotive sector. A simulation model based on the finite element method is proposed. For the modelling of the polymeric material, the three-network viscoplastic (TNV) rheological model was used, with very adequate results and producing a good fit with the experimental data. In addition, a methodology is proposed that allows simplifying a three-dimensional to an axisymmetric model, which implies a notable reduction in computational cost. In addition, the work includes an experimental analysis that evaluates the tightening torque under conditions of assembly repetitiveness, relaxation over time and influence of thermal cycles. These scenarios have a different influence depending on the geometry of the self-tapping screw used. Regarding repetitiveness, it has been verified that PF-30 (CELOspArk®) loses 17.16% while in Δ-PT (DELTA PT®) it loses up to 41.93% in the tenth repetition. In contrast, in the relaxation over time scenario, the PF-30 loses 13.38% and the Δ-PT loses 17.82%. Finally, regarding the thermal cycles, cooling allows to slightly delay the loss of tightening torque in both screws in a similar way; however, in the heating stage, 36.89% is lost with PF-30 and only 14.66% with Δ-PT. This study represents an improvement in the knowledge of the joining processes of self-tapping screws with polymeric materials of an engineering nature. The simulation model can be easily adapted to other materials and other geometries, and the experimental study offers a vision of the evolution of tightening conditions in realistic operating scenarios.

Keywords Automotive component joints · Rheological model · PEI · FEA · Loosing torque

1 Introduction

Polymeric materials are essential in today's automotive industry and are present in numerous parts, such as bumpers, dashboards, trims, gaskets, headlights and taillights. A current car owes approximately 20% of its weight to these materials [1, 2].

There are many polymeric materials, so for an appropriate choice it is necessary to know the characteristic properties and the environment where they are going to be used. In general, a polymer used in the automotive industry is made up of macromolecules formed by sequences of carbon and hydrogen atoms, between which silicon, nitrogen, oxygen and sulphur atoms can be intercalated, joined by covalent bonds, constituting a linear or reticulated molecular chain [3]. The molecular weight of the macromolecules is not always the same since the number of molecules that are grouped in the polymerization reaction is determined by random circumstances, for which an average molecular weight, degree of polymerization and an index of polymerization are usually to characterize them. For most industrial uses, there is an upper molecular weight limit above which the tensile strength and refractive index decrease dramatically [4].

Unlike its molecular structure, which cannot be modified without breaking its covalent bonds, the shape and arrangement of the chains can be varied by physical means such as mechanical stress or thermal variations [5]. In the solid state, the molecular chains are intertwined in a disorderly manner, constituting the so-called amorphous matrix, or they are packed in an orderly manner, forming crystalline zones. Normally crystalline and amorphous zones coexist in polymers [6].

In order to improve the behaviour of polymers against mechanical and thermal stresses, additives and fibre glass are often used [7]. Thus, for example, to protect against

✉ Wilmer E. Cumbicus
wilmer.cumbicus@upct.es

[1] Mechanical, Material and Manufacturing Engineering, Universidad Politécnica de Cartagena, 30202 Cartagena, Spain

[2] School of Engineering, TECNUN, Universidad de Navarra, Pº de Manuel Lardizabal 13, 20018 Donostia-San Sebastián, Spain

degradation phenomena, molecular stabilizers and ultraviolet radiation absorbers are used. In some cases, plasticizers are used so that the polymer acquires a certain flexibility [8]. To confer colour and facilitate fluidity during the manufacturing process, dyes and lubricants are used. When you want to provide mechanical resistance and rigidity, reinforcing fibres are used, which in the manufacture of bodywork elements are generally glass, presenting themselves in the form of long fibres, felts, chopped threads, etc. [9].

When it comes to joining polymer parts, one of the cheapest methods that guarantees stability and durability of the joint is the use of metal self-tapping screws [10–12]. In most cases, self-tapping screws should allow repetitive assembly and disassembly of polymeric parts without substantially losing joining capabilities and without the need to change screw dimensions.

Most of the published studies on thread forming screws are based on experimental results using bosses or metal plates [13–17]. There are few works that are accompanied by numerical modelling of polymeric materials, largely due to the difficulty of modelling this type of material.

Seneviratne et al. [18, 19] investigated a wide variety of polymers (in particular they analysed polypropylene, acrylonitrile butadiene styrene and polycarbonate), assembled using steel screws. These studies were based on the analytical development of a quasi-static analysis. They found an acceptable correlation between the data obtained from their analytical model and those obtained experimentally.

Ellwood et al. [20] presented for the first time a model based on FEM to try to elucidate the process of forming threads in a polycarbonate and polypropylene insert using steel screws. To model the polymeric materials, the authors resorted to the Eyring theory and obtained consistent results despite making many simplifications in terms of material, process, geometry and operation.

The selection of rheological models of materials that approximate the behaviour of the polymer is a critical issue [21], and it is evident that a complex constitutive model allows a better reproduction of the real behaviour. In this sense, Arruda and Boyce [22] evaluated the capabilities of various rheological models to predict the response state over a range of temperatures and bounded strain rates. The models were based on three main elements: a linear spring, a viscous damper and a nonlinear rubber elasticity spring. Models successfully predicted moderate stress and strain rates with data obtained from isothermal uniaxial compression and plane stress compression experiments. Subsequently, Tomaš et al. [23] developed a simple implicit formulation of the Arruda-Boyce viscoplastic model. The formulation makes use of a backward Euler scheme in combination with standard procedures for updating the stresses in the relaxed configuration. This implementation was defined as a user-defined material routine in the ABAQUS-Standard environment.

Other researchers such as Arriaga et al. [24] found a correlation between the results of experimental mechanical tests on thermoplastic materials and numerical simulations based on multilinear isotropic hardening and multilinear kinematic hardening using the ANSYS© finite element code.

The constant development of new polymeric materials with very good mechanical, thermal and electrical properties, etc., represents an important challenge in the search for rheological models for numerical simulations that can reproduce the behaviour of polymers under load states. In this sense, Bergström and Bischoff [25] developed an advanced thermomechanical constitutive model for ultra-high molecular weight polyethylene (commonly referred to as UHMWPE). In the model, the microstructure of the material is represented using three different structural domains that capture the nonlinear response, dependent on time and temperature, observed experimentally in both small and large strains.

More recently, Sepiani et al. [26] presented a finite element implementation of constitutive viscoelastic and viscoplastic models for the prediction of long-term behaviour of polymers. The method is presented for small strains, but it is extended to large strains in which the stress–strain relationship is not linear, and the concept of incompressibility governs. An empirical approach is used to determine material parameters in constitutive equations, based on measured material properties. The modelling process uses a spring and damper and a power law approximation function method for nonlinear viscoelastic and viscoplastic behaviour, respectively.

A review of the literature revealed that a correct modelling of the polymeric material is essential to be able to estimate its behaviour accurately. It is especially important when the polymer is going to be subjected to mechanical and thermal stresses, as these properties turn out to be very sensitive to sudden variations and can compromise the safety of the assembled parts. Therefore, the purpose of this work is to develop, on the one hand, a numerical simulation model based on the finite element method. This model must use an advanced rheological model by the polymeric material, providing robustness to the results, but it be a simplified as possible in geometric terms to achieve satisfactory results with a low computational cost. The model will be able to predict the behaviour of self-tapping joints between metal screws and polymeric parts with high mechanical performance, such as the fibre glass reinforced polyetherimide (trade name is ULTEM™ Resin AUR 200G6, we refer to hereinafter this material as PEI) resin, which is increasingly used in automotive applications.

On the other hand, to analyse this type of self-tapping joints under different realistic scenarios to which the assembled components may be subjected throughout their useful life, such as the relaxation over time, the repeatability of the assembly and the effect of thermal cycles. All this considering the geometry of the self-tapping screw.

2 Experimental procedure

In order to carry out the experimental tests efficiently from the point of view of material consumption, several specimens (see Fig. 1) were prepared to represent the real part assemblies. The boss material corresponds to PEI with great dimensional stability, high stiffness/strength and high temperature resistance. All polymeric specimens were designed with a hole diameter (d_L) an 80% smaller than the nominal diameter of the screws (d_1) and conicity angle of 5.5°. These and other parameters can be consulted in Table 1. The thickness plate has been 11 mm.

Two different families of self-tapping screws with the following trade names were chosen: "PF-30" (CELOspArk®) and "Δ-PT" (DELTA PT®) (see Fig. 2). These screws were made of AISI 19MnB4 steel with a thread pitch of 2.24 and 1.8 mm, respectively. Various diameters and lengths of screws were tested; however, the present study focuses on screws with a nominal diameter of 5 mm due to their large volume of use in the assemblies of polymeric parts in the automotive industry.

The experimental tests have been divided into two parts. In the first part, the torque and clamping force were measured throughout the assembly process. An automatic screwdriver with a rotation capacity of up to 1200 rpm was used for the assembly process. The torque was measured using a torque sensor with a measurement range of 0–15 N·m and an uncertainty of 1%. For the clamping force, a load cell with a measurement range of 0–7.5 kN with an uncertainty of 0.5% was used. The load cell has a through hole so as not to interfere with the assembly process and was placed between the screw and boss. The experimental tests were controlled using the VCI PC 1.30.1.4 software, where the rotation speed and the data acquisition time were configured.

In the second part, the same devices described above were used, but this time the loosening torque was measured to evaluate the effectiveness of tightening the screws with the PEI polymeric boss. The loosening torque was evaluated against repeatability of assemblies, evolution over time and thermal cycles. In order to obtain a representative average value, 10 repetitions were performed for each of the considered stages. For the thermal cycle, a freezer was used first, reaching − 20 °C and remaining for up to 2 h; for the heating phase, an oven was used, brought to 80 °C, and also remaining for 2 h.

Table 1 Self-tapping screws' parameters

Parameters	PF-30 (CELOspArk®)	Δ-PT (DELTA PT®)
d_1	5.00	5.00
d_r	3.36	3.22
β	30	30
β'	–	20
p	2.24	1.80

3 Finite element model

3.1 Approximation of the screwing process

To reduce the complexity of solving a fully three-dimensional formulation and since the thread forming length is reasonably small compared to the screw diameter, the following approximation was used: one revolution of the helix was made to correspond to a circular hoop. In this sense, the visualization process of the problem becomes axisymmetric as shown in Fig. 3 (this geometry corresponds to

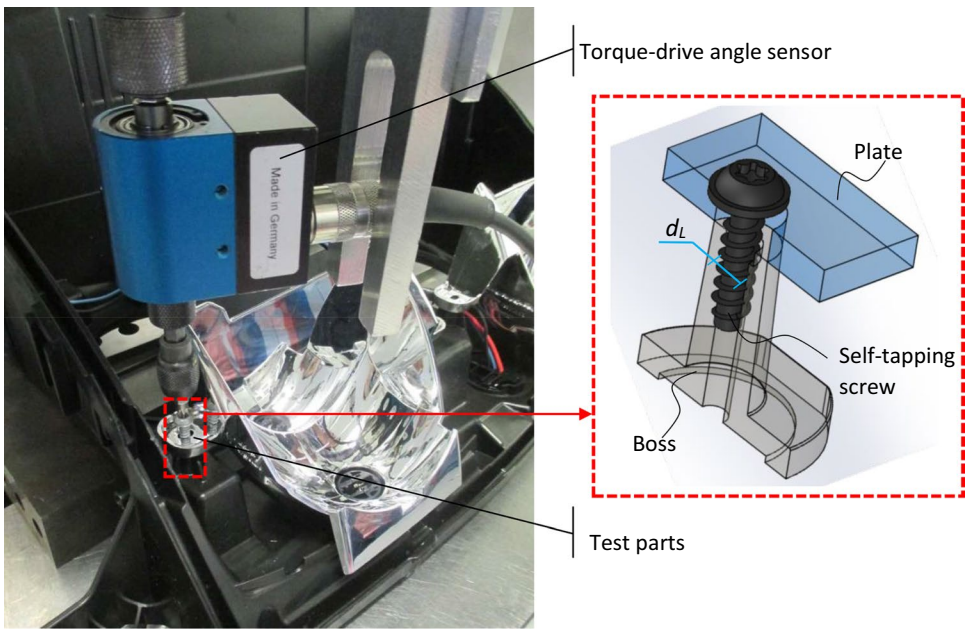

Fig. 1 Devices for measuring experimental test and tested parts

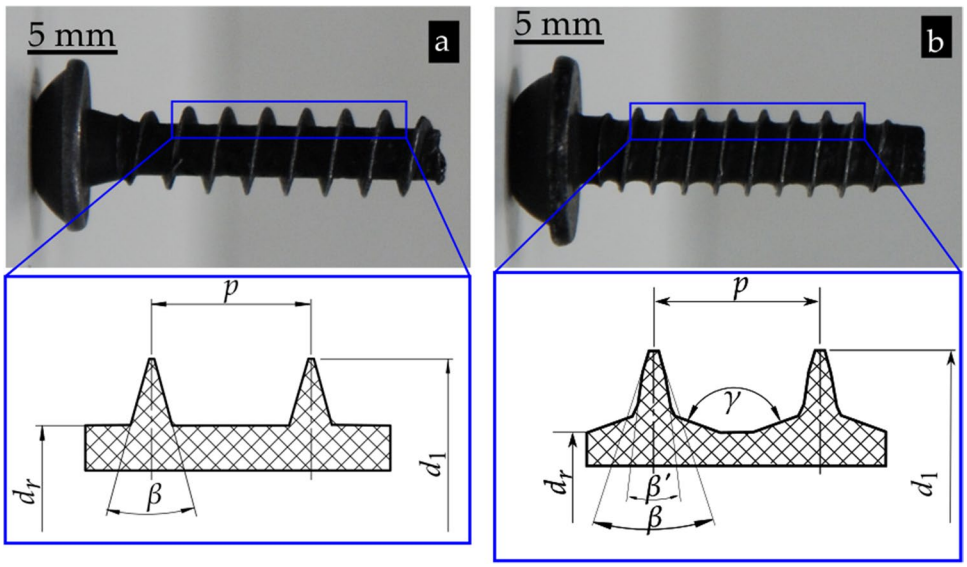

Fig. 2 Tested self-tapping screws: **a** PF-30 and **b** Δ-PT

PF-30), where the equivalence of one helical thread and the next can be seen as a series of hoops arranged one after the other.

As the screws have a taper at the beginning of the thread, some more than others, until they reach the nominal diameter, the first hoop will penetrate a smaller radial distance than the next on the boss and so on successively until reaching the nominal diameter. Once the nominal diameter is reached, the successive hoops will penetrate the same radial distance. Radial distance, in such a way that for the screw represented in Fig. 3 the circumferential advance of the thread can be approximated as a progressive radial penetration. Three instants have been represented for the first hoop, initial (red), intermediate (fuchsia) and final (cyan). The second hoop goes a little deeper than the first, turning from cyan to blue after one full turn. The third and subsequent hoops, which are no longer

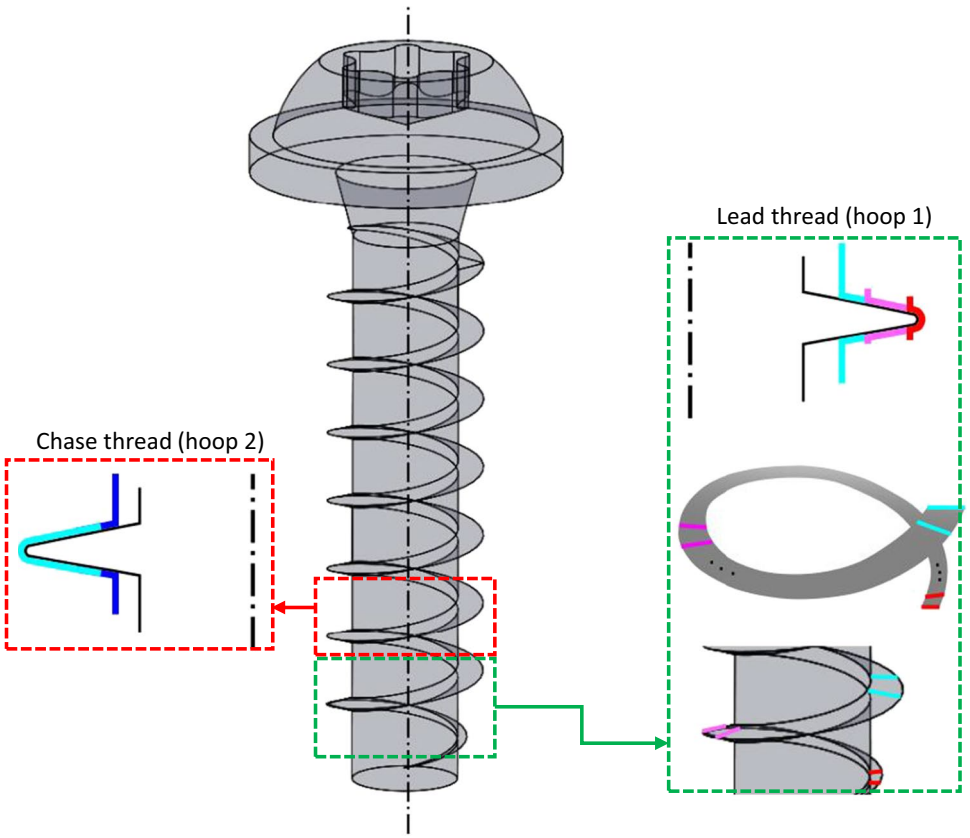

Fig. 3 Helical thread approximation. This geometry corresponds to PF-30 self-tapping screw

represented in Fig. 3, will simply displace the material that has recovered the polymer, mainly due to elastic recovery.

To represent the advance between hoops and, therefore, the advance of the screw, these are displaced axially a distance equivalent to the pitch of the screw. The first hoop starts again to completely generate a new thread in an undeformed area of the boss and the rest of the hoops will occupy already deformed positions.

To represent the dynamics of the screw thread forming in the boss, the methodology presented in [27] has been followed, as summarized below:

1. *Start*. The thread of the screw is positioned in the place where the thread will be generated.
2. The thread is advanced radially displacing material from the boss.
3. The thread is moved back to the initial position marked point 1.
4. The thread is advanced a distance equal to the pitch of the screw.
5. Repeat steps 1 to 4 until all the hoops have penetrated the boss.
6. All the hoops move axially, compressing the material against the screw head. *End*.

3.2 Description of FEM

The model described above was solved using the Abaqus Explicit solver corresponding to the commercial finite element software Abaqus©. Due to the adiabatic conditions of high assembly speed, where the heat transfer is minimal, they were assumed for the simulation. The application of explicit dynamics to model quasi-static systems with the thread forming process in its natural time period is computationally impracticable. Literally millions of time increments are needed. Therefore, the mass scaling approach has been used to artificially increase the speed of the process in the simulation to obtain a computationally cheap solution. All bodies were generated and meshed within the Abaqus/CAE 2016 environment.

The bodies defined in the simulation model are the discretized screw in the hoops and the independent head, and the boss where the thread will be formed. The load cell (corresponding to plate) has been omitted since this body is only used in the experimental measurements to determine the clamping force and, therefore, equal friction between the screw-boss and load cell-boss surfaces is assumed.

Friction along the contact interface of thread components during the assembly process is a very complex phenomenon and influences tool geometry, temperature and wear. In this work, a

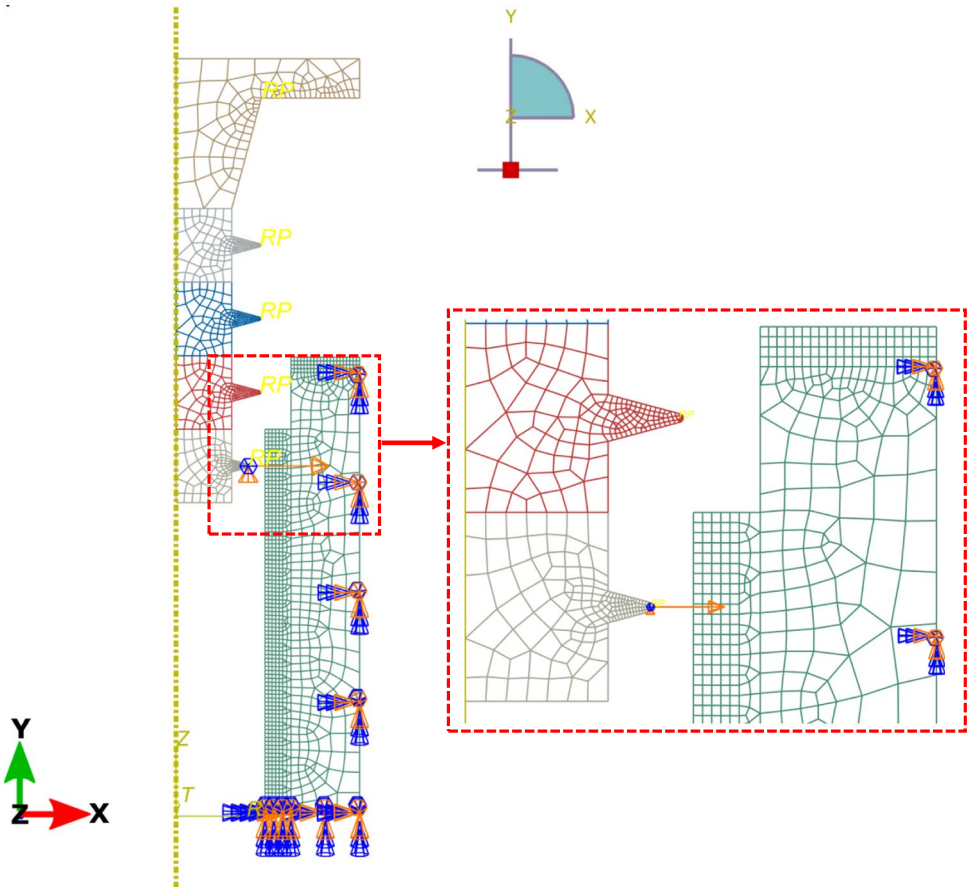

Fig. 4 Finite element model (this geometry corresponds to PF-30)

simple Coulomb friction model was assumed for all interacting surfaces. In this model, the general contact algorithm with a finite sliding contact reinforces the contact interactions between all the bodies in the model. Contact restrictions were applied using the penalty method.

All screw entities were assumed to be rigid bodies, which allowed boundary conditions to be applied independently using a single reference point of each discretized entity. Consequently, the degrees of freedom of the model are substantially reduced. On the contrary, the boss was the only body that was considered deformable.

At the base of the boss, movement in all directions was restricted. An XSYMM boundary condition was applied to the external wall of the boss. These boundary conditions were defined in the initial step and propagated until the last step.

The reference point of the screw head was constrained in all directions. This condition was defined in the initial step and propagated until completing the last step of the thread forming phase and is only modified in the tightening phase to compress the boss on the upper face. On the contrary, the reference points of the hoops were defined and modified to allow the dynamics described in the previous section in both phases of the tightening process.

The meshing of the boss was carried out keeping in mind a high density of elements in the zone of large deformations. The internal and external zones were meshed with bilinear quadrilateral elements with reduced integration and hourglass control (CAX4RT), and for the transition between these zones, linear triangular elements (CAX3T) were used, which are available in the Abaqus element library [28]. Likewise, both the screw head and the hoops were meshed with CAX4RT and CAX3T elements. In total, the whole model has 29,228 elements, of which 28,163 correspond to the boss and the rest to the threads and the screw head. In all simulations, attention was paid to the energy balance to ensure energy conservation in the numerical model during the assembly process of the quasi-static system. The average CPU time of the simulations was 29 h using a computer with 8 cores Intel(R) Core at 2.50 GHz with 8 GB DDR 2933 MHz of RAM.

Table 2 Thermomechanical properties of screw

Properties	Steel (AISI 19MnB4)
Density ρ (g cm^{-3})	7.83
Elastic modulus E (MPa)	210,000
Poisson's ratio ν (–)	0.29
Specific heat C_p (J g^{-1} °C^{-1})	0.475
Thermal conductivity k (W m^{-1} °C^{-1})	44.5
Thermal expansion α_T (µm m^{-1} °C^{-1})	13.2

Figure 4 shows the meshing and the boundary conditions defined in its initial step.

The behaviour of the elastic material of the self-tapping screw with Young's modulus and Poisson's ratio of 210,000 MPa and

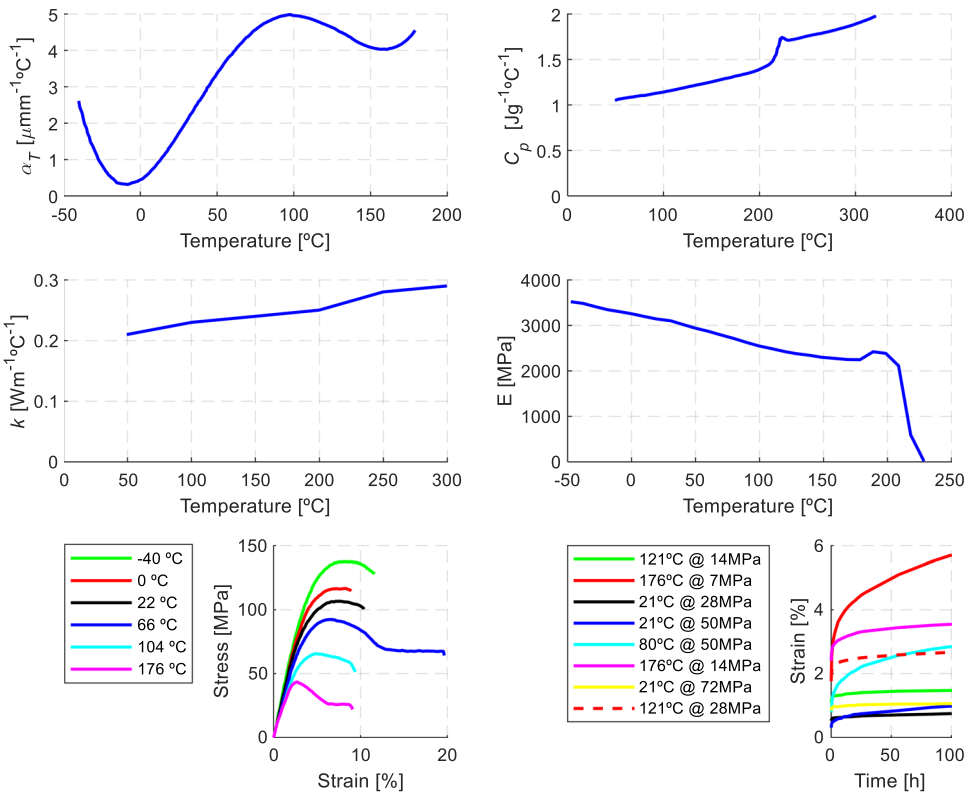

Fig. 5 Thermal and mechanical properties of PEI with 30% fibre glass reinforced

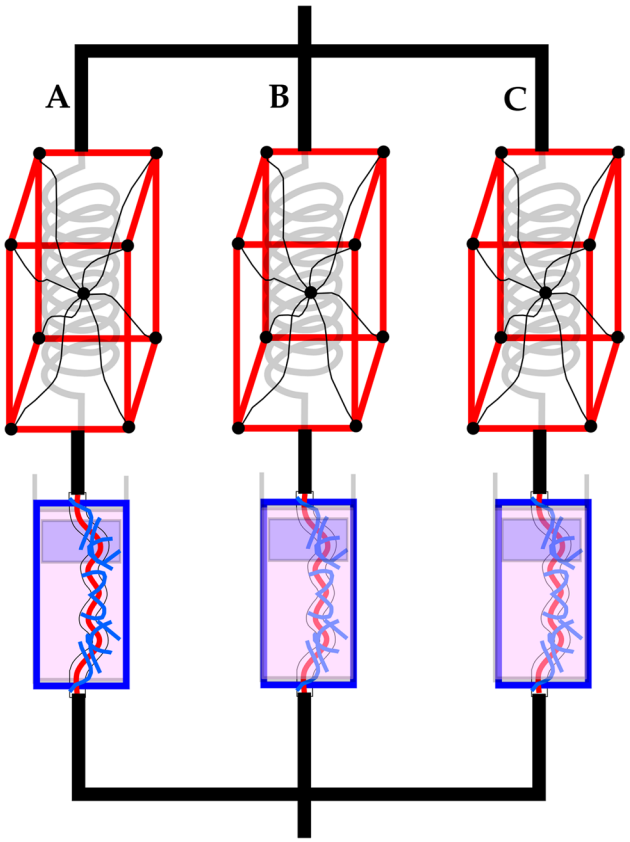

Fig. 6 Rheological model of polymer bosses (**A**, **B** and **C** correspond to the three parallel networks)

0.29, respectively, was assumed. The mechanical and thermal properties of the AISI 19MnB4 steel with which the screws were manufactured are shown in Table 2, while the PEI boss was modelled following the curves shown in Fig. 5. To calibrate the behaviour of the polymeric material, the MCalibration® tool was used [29], which uses the three-network viscoplastic (TNV) model described in the following section.

3.3 Modelling of the polymeric material

The TVM model consists of three parallel networks (Fig. 6). The total strain gradient $\boldsymbol{F}$ acts on all three networks: $\boldsymbol{F}=\boldsymbol{F}_A=\boldsymbol{F}_B=\boldsymbol{F}_C$, and the total Cauchy stress is given by the sum of the three branches: $\boldsymbol{\sigma}=\boldsymbol{\sigma}_A+\boldsymbol{\sigma}_B+\boldsymbol{\sigma}_C$.

3.3.1 Behaviour of the hyperelastic network

The three networks (A, B and C) are based on the same constitutive equations, so the development will not be segregated for any in particular. Viscoplastic strain gradient acting on a network decomposes into elastic and viscoplastic parts [30], as shown in Eq. 1:

$$\boldsymbol{F}=\boldsymbol{F}^e\boldsymbol{F}^v \tag{1}$$

The Cauchy stress acting on a network is given by the Yeoh model [31] with Cauchy stress as shown in Eq. 2:

$$\begin{aligned}\boldsymbol{\sigma}=&\frac{2f_\epsilon\cdot\eta}{J^e}\left\{C_{10}+2C_{20}\left(I_1^*-3\right)+3C_{30}\left(I_1^*-3\right)^2\right\}\mathrm{dev}\left[\mathbf{b}^*\right]\\&+\left[\kappa_1(J^e-1)+\kappa_2(J^e-1)^3+\kappa_3(J^e-1)^5\right]1\end{aligned} \tag{2}$$

3.3.2 Flow network behaviour

The viscoplastic flow velocity gradient of network A can be written as shown in Eq. 3:

$$\dot{\mathbf{F}}_A^v=\dot{\gamma}_0\left[R\left(\frac{\tau_A}{f_pf_{\epsilon p}\widehat{\tau}_A}-0.001\right)\right]^m\mathbf{F}_A^{e-1}\left[\mathbf{N}_A+b\mathrm{sign}(tr[\boldsymbol{\sigma}])1\right]\mathbf{F} \tag{3}$$

where:

- $\left[\widehat{\tau}_A,m\right]$ are material parameters.
- $\dot{\gamma}_0\equiv\frac{1}{s}$ is a constant introduced for dimensional consistency.
- The effective stress driving viscoplastic flow is given by the deviatoric Hill stress represented in Eq. 4.

$$\tau_A=\left[F\left(\sigma'_{A.22}-\sigma'_{A.33}\right)^2+G\left(\sigma'_{A.33}-\sigma'_{A.11}\right)^2+H\left(\sigma'_{A.11}-\sigma'_{A.22}\right)^2+2L\sigma'^2_{A.23}+2M\sigma'^2_{A.31}+2N\sigma'^2_{A.12}\right]^{\frac{1}{2}} \tag{4}$$

- The $\mathbf{N}_A$ tensor specifies the direction of the driving deviatoric stress from the convectively relaxed configuration to the current configuration according to Eq. 5.

$$\mathbf{N}_A=\frac{\mathrm{dev}\left[\boldsymbol{\sigma}_A\right]}{\tau_A} \tag{5}$$

- The term $b\mathrm{sign}(tr[\boldsymbol{\sigma}])1$ gives rise to volumetric viscoplastic flow, where b is a material parameter.
- The pressure dependency of the viscoplastic flow is captured by the function reported in Eq. 6.

$$f_p=\begin{cases}max\left(0.5,1+p_0\frac{p}{\widehat{\tau}_A}\right),if p_0>0,\\max\left(0.5,1-p_0\frac{p}{\widehat{\tau}_A}\right),if p_0<0 and p<0,\\1,otherwise\end{cases} \tag{6}$$

where $p=-\frac{1}{3}\mathrm{tr}\left[\boldsymbol{\sigma}_A+\boldsymbol{\sigma}_B+\boldsymbol{\sigma}_C\right]$ is the hydrostatic pressure. In summary, if $p_0>0$, then the yield stress is reduced in a state of tensile pressure and increased in a state of compressive pressure, and if $p_0<0$, then the yield stress is only reduced in a tensile pressure state.

- Since the resistance to flow evolves with the plastic deformation, the specific yield evolution function $f_{\varepsilon p}$ is defined according to Eq. 7.

$$f_{\varepsilon p} = f_f + (1 - f_f)\exp\left[\frac{-\varepsilon_p}{\varepsilon_f}\right] \tag{7}$$

where $f_{\varepsilon p}$ is the von Mises strain obtained from $\mathbf{F}_A^v$ and $[f_f, \varepsilon_f]$ are material parameters.

3.3.3 Strain-based failure predictions

The strain-based failure condition for the material model is given by Eq. 8:

$$\varepsilon_H(t) = \left\{\frac{2}{9}\left[F(\varepsilon_{22} - \varepsilon_{33})^2 + G(\varepsilon_{33} - \varepsilon_{11})^2 + H(\varepsilon_{11} - \varepsilon_{22})^2\right] + \frac{4}{3}\left[L(\varepsilon_{23})^2 + M(\varepsilon_{31})^2 + N(\varepsilon_{12})^2\right]\right\}^{\frac{1}{2}} > \varepsilon_{fail} \tag{8}$$

where ε_H is strain Hill and ε_{fail} is the failure strain given by Eq. 9:

$$\varepsilon_{fail} = G(\sigma_{triax})\left\{\frac{f_{es} - f_{ef}}{2}\left[1 - \operatorname{erf}\left(\frac{\ln\left|\frac{\dot{\varepsilon}}{f_A}\right|}{f_B}\right)\right] + f_{ef}\right\} \tag{9}$$

3.3.4 Stress-based failure predictions

The stress-based failure condition for the material model is given by Eq. 10:

$$\sigma_H(t) = \left[F(\sigma_{22} - \sigma_{33})^2 + G(\sigma_{33} - \sigma_{11})^2 + H(\sigma_{11} - \sigma_{22})^2 + 2L\sigma_{23}^2 + 2M\sigma_{31}^2 + 2N\sigma_{12}^2\right]^{\frac{1}{2}} \geq \sigma_{fail} \tag{10}$$

where σ_H is the Hill stress and σ_{fail} is the failure stress given by Eq. 11:

$$\sigma_{fail} = G(\sigma_{triax})\left\{\frac{f_{es} - f_{ef}}{2}\left[1 - \operatorname{erf}\left(\frac{\ln\left|\frac{\dot{\varepsilon}}{f_A}\right|}{f_B}\right)\right] + f_{ef}\right\} \tag{11}$$

4 Results and discussions

In this section, both the numerical simulations and the experimental results are presented and discussed.

First, according to analytical studies, like the one developed in [32], it is recommended that to avoid premature failures when polymers are assembled with self-tapping screws, the tightening torque should be within the range given by Eq. 12:

$$T_t = T_i + \frac{1}{2}\cdots\frac{1}{3}(T_s - T_i) \tag{12}$$

where:

- T_t is the tightening torque.
- T_i is the installation torque, which is the result of the sum of the forming torque and thread friction.
- T_s is the stripping torque, which is the limit torque from which the joint becomes unstable.

In this context, to consider the torque due to friction in numerical simulations, experimental tests have been used to determine the coefficient of friction according to the simplified Coulomb model. The following section develops the methodology followed.

4.1 Obtaining the coefficient of friction

To determine the coefficient of friction between self-tapping screws and the PEI polymer, the following procedure has been followed:

- Once the torque–angle characteristic curve is known, the boss is screwed up to a tightening torque of 1/2 of the T_s-T_i section, considering Eq. 12.
- The screw is completely unscrewed.
- It is screwed in a second time on the same boss and both the tightening torque and the clamping force are recorded. These data are taken as representative.

Table 3 Friction coefficients obtained experimentally

Test	T_t^*(Nm)	F_v(kN)	μ(–)
1	3.37	1.55	0.41
2	3.38	1.56	0.40
3	3.39	1.57	0.38
4	3.37	1.55	0.43
5	3.40	1.58	0.43
Average	3.38	1.56	0.41

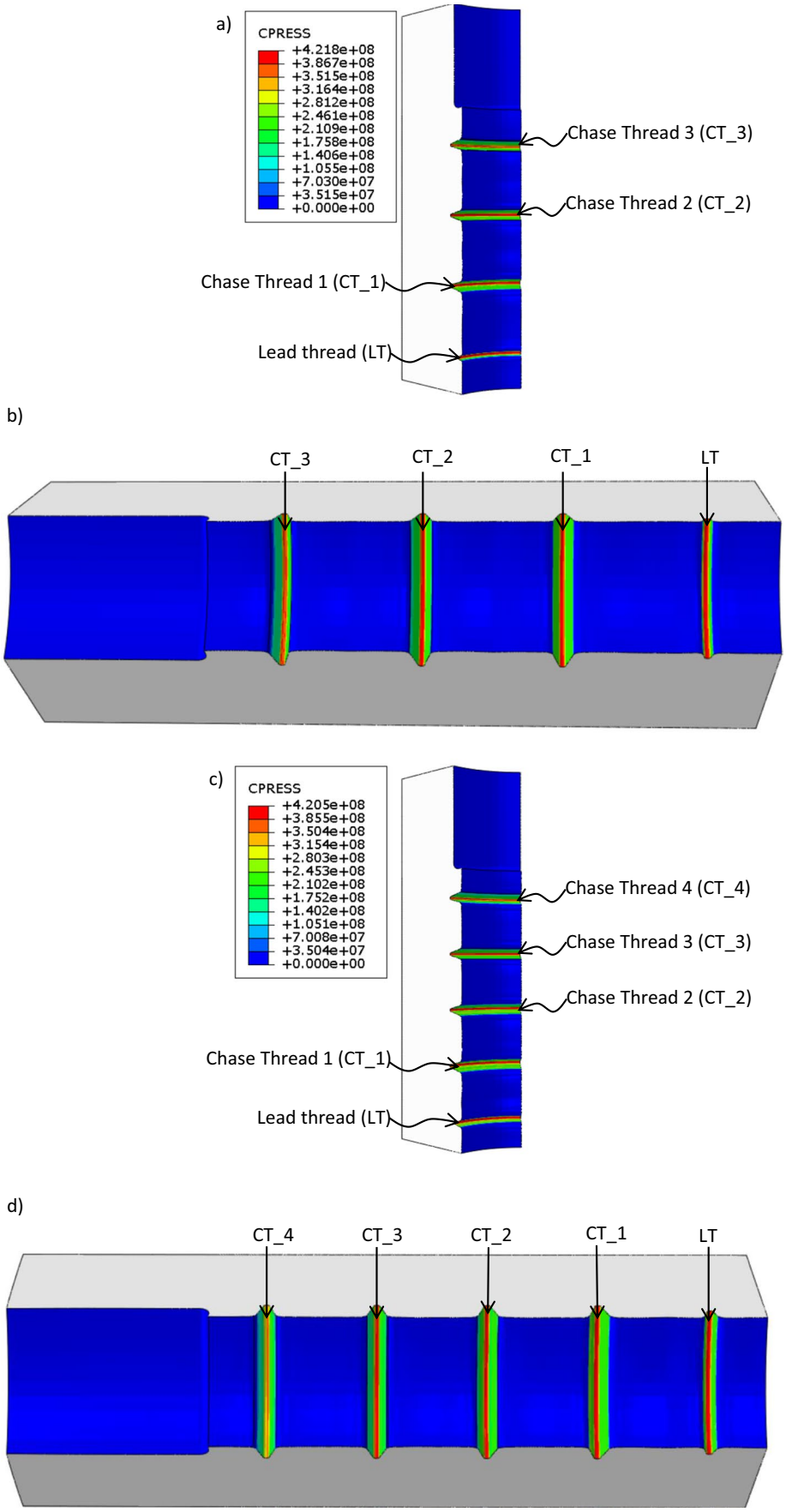

Fig. 7 Contact pressures at the end of the thread forming phase: **a** inside boss with PF-30, **b** detail **a**, **c** inside boss with Δ-PT and **d** detail **c**

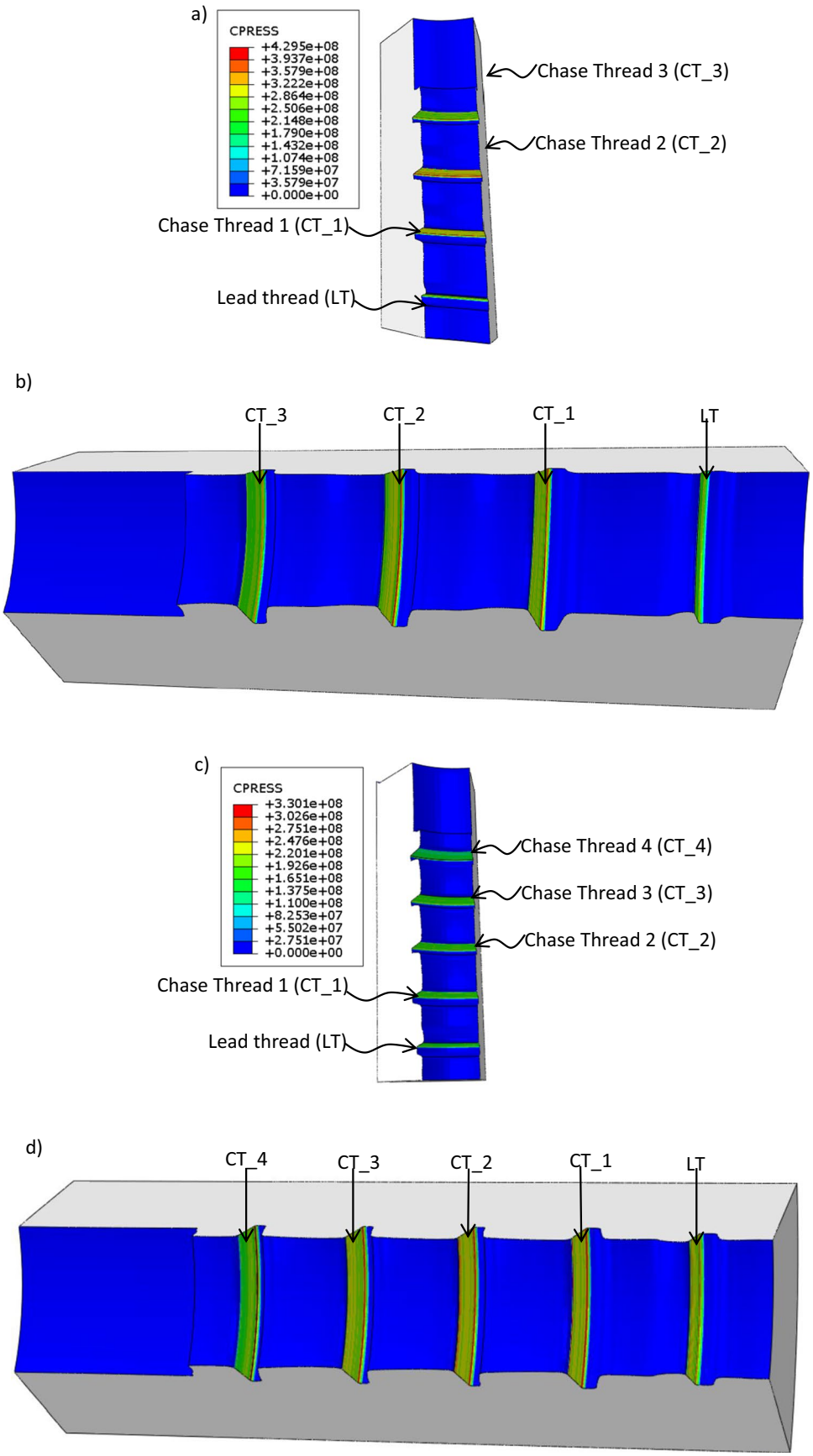

Fig. 8 Contact pressures at the end of the tightening phase: **a** inside boss with PF-30, **b** detail **a**, **c** inside boss with Δ-PT and **d** detail **c**

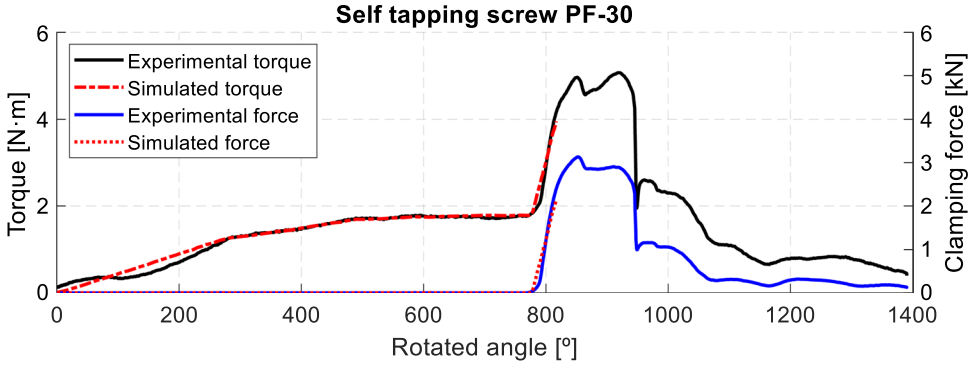

Fig. 9 Experimental vs simulated values of torque and force using PF-30

- It is repeated five times and average of tightening torque and preload force is obtained.

Under these conditions, it can be considered that the tightening torque T_t^* is composed of the torque due to friction in the thread T_{GR} and the torque due to friction between the screw head and the boss T_{KR} according to Eq. 13:

$$T_t^* = T_{GR} + T_{KR} \tag{13}$$

On the one hand, the friction torque of the thread can be calculated according to Eq. 14:

$$T_{GR} = F_v \frac{d_m}{2} \tan\left(\beta + \rho_G\right) \tag{14}$$

where $\beta = \arctan\left(\frac{p}{\pi d_m}\right)$, $d_m = \frac{d_1 + d_k}{2}$ and $\rho_G = \arctan\left(\frac{\mu_G}{\cos\left(\frac{\alpha}{2}\right)}\right)$.

On the other hand, the friction torque of the screw head with the boss can be calculated according to Eq. 15:

$$T_{KR} = F_v \frac{d_M}{2} \tan\left(\rho_K\right) \tag{15}$$

where $d_M = \frac{d_S + d_A}{2}$, with d_S and d_A as the inside and outside diameter of the surface that comes into contact with the screw head, respectively.

$$\rho_K = \arctan\left(\mu_K\right)$$

μ_G and μ_K represent the friction of the screw thread and the friction of the screw head with the boss, respectively.

Therefore, substituting values for the tightening torque under the conditions described above, Eq. 16 is obtained:

$$T_t^* = F_v \left[\frac{d_m}{2} \tan\left(\beta + \rho_G\right) + \frac{d_M}{2} \tan\left(\rho_K\right)\right] \tag{16}$$

In this sense, the only two unknown variables are μ_G and μ_K. Assuming that $\mu_G = \mu_K = \mu$, a nonlinear equation with a single unknown is obtained, the results of which are shown in Table 3.

4.2 Obtaining the tightening torque and the clamping force

Next, the contact pressures produced during the two main phases involved in the process are shown: the thread forming phase and the tightening phase for both families of simulated screws.

Figure 7 shows the pressure generated by all the threads at the end of the thread forming. (In terms of torque, it would be the instant at which the so-called installation torque is completed according to Eq. 12). In Fig. 8, the contact pressure at the end of tightening up to the simulated point has been represented, which has been 2/3 of the distance between T_s-T_i.

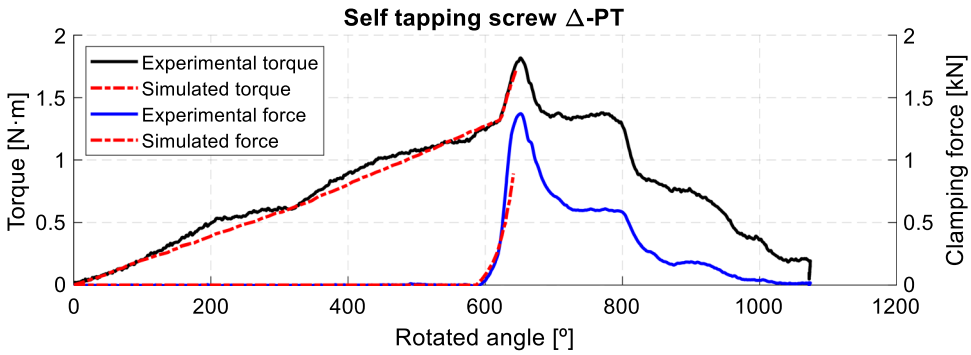

Fig. 10 Experimental vs simulated values of torque and force using Δ-PT

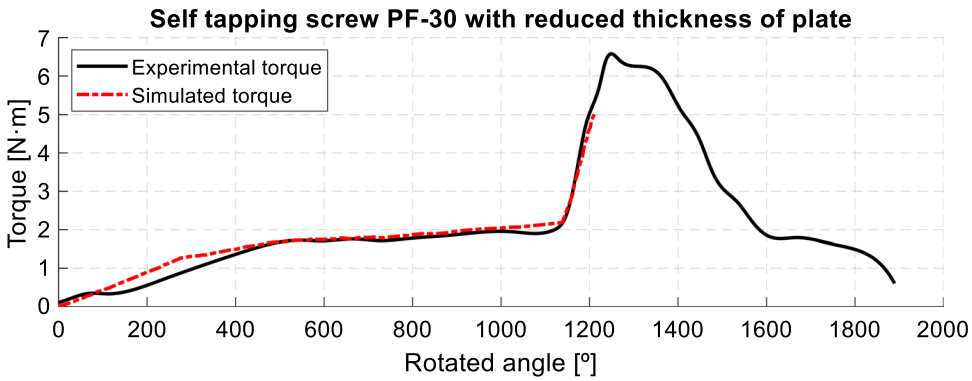

Fig. 11 Experimental vs simulated values of torque using PF-30 with reduced thickness of plate

Regarding the thread forming phase, the pressure results reveal that the maximum pressure is produced by the tip of each thread and, therefore, the bottom of the generated polymeric thread. Of all the threads, the lead thread, which is the one that performs the greatest work of plastic deformation, is the one that generates the greatest pressure. On the contrary, the chase threads provide less pressure largely because their objective is to slightly increase the deformation previously carried out by the lead thread and hold the material and rub, serving as a blocker of the elastic recovery fraction of the polymer.

The pressures are quite similar for each of the screws used; however, it can be noted that in the case of the PF-30 screw, due to its smaller tip and longer flank length than the Δ-PT, it produces a higher pressure. In the Δ-PT screw, due to its geometry, once the tip has entered, the polymeric material offers less resistance, so its final pressure in the thread forming stage is lower than that of PF-30.

As for the tightening phase, the behaviour follows the same trend as the previous stage, obtaining a lower pressure in the case of the Δ-PT screw compared to PF-30.

With the pressure data in each of the phases, the torque generated in an axisymmetric system was determined using Eq. 17.

$$T_t = \mu \iint r^2 p ds d\theta \tag{17}$$

where p is the pressure transmitted across the contact interface, r is the radius to a point on the interface, s is the current distance along the interface in the R-Z plane, and θ represents degrees rotated along the helix.

Figures 9 and 10 show the numerical and experimental results of the thread forming process in bosses with a hole of $d_k = 4.0$ mm using both families of self-tapping screws.

The experimental torque–angle and clamping force-angle curves correspond to the average curve resulting from 10 assemblies under the same conditions.

According to the torque–angle and clamping force-angle curves, an adequate correlation between the experimental data and the plots from the numerical simulations is observed.

By incorporating the load cell to register the tightening force in bolted joint tests, the length of the screw that generates the thread inside the boss is substantially reduced (curves shown in Figs. 9 and 10). In these graphs, it is equivalent to performing a tightening with a plate of thickness equal to that of the load cell, which in this case was 11 mm. According to the study carried out in [27], where screws with a length of 24 mm were used, the evolution of the tightening force evolves proportionally to the torque.

Figures 11 and 12 show the torque–angle curves obtained experimentally and simulated, taking into account that the length of the screw goes from 20 to 24 mm, which is equivalent to reducing the thickness of the plate from 11 to 7 mm. The graphs show some interesting aspects that are discussed below.

In the thread forming phase, the linear increase in torque due to the increase in the number of threads is much more

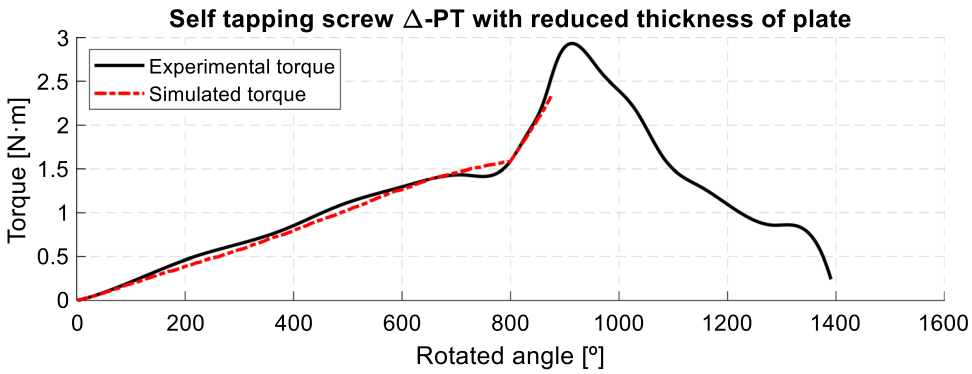

Fig. 12 Experimental vs simulated values of torque using Δ-PT with reduced thickness of plate

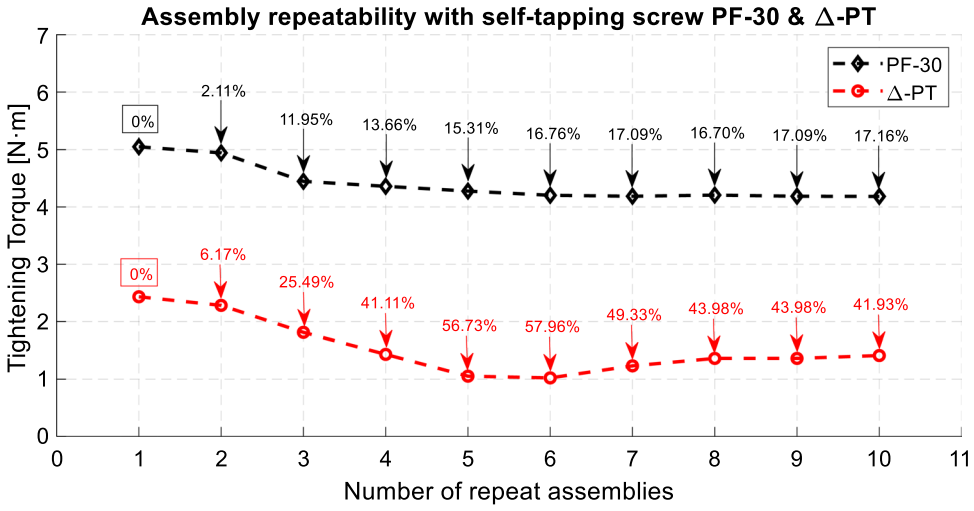

Fig. 13 Loosing tightening torque using PF-30 and Δ-PT

evident in the case of the Δ-PT screw geometry, while in the case of PF-30 it barely increases compared to that obtained with a thickness of 11 mm. This is due to a shorter friction length, as this last screw has a greater pitch.

A similar phenomenon occurs in both assemblies. The evolution of the thread forming torque reaches a maximum point, after which it tends to decrease. This phenomenon is interpreted as follows: there is a maximum thread length that generates heat due to friction, but beyond that maximum thread length, the polymeric material tends to offer less resistance, favouring the flow of the material according to the geometry of the screw. This phenomenon could not be registered in the numerical simulations.

In the tightening phase (understood as the section of the curve between T_s-T_i), the torque increases linearly in both configurations. In percentage terms, there is a clear difference between Δ-PT and PF-30. In the case of Δ-PT, there is an increase of 152%, while in the case of PF-30 there is an increase of 45%. Numerically, in the case of Δ-PT, it goes from 0.594 to 1.459 Nm and in the case of PF-30, from 3.163 to 4.583 Nm. As a consequence of the torque improvement, the tightening force will improve substantially when the Δ-PT screw is used on the polymer; however, it is far from the values obtained in PF-30.

In addition to what was discussed in the previous paragraphs, the Δ-PT screw has a significant advantage when the plate thickness is reduced. It can be seen that the slope of the torque–angle curve of the tightening phase is less than that obtained with the PF-30 screw.

Consequently, it provides a greater guarantee of successful assemblies and offers greater ease when establishing a rotation limit in the screwing machines that are frequently used in the assembly of automobile parts.

4.3 Evaluation of repeatability in assemblies

The objective of this test is to determine the ability of both families of screws to maintain joint performance during various repetitive assemblies.

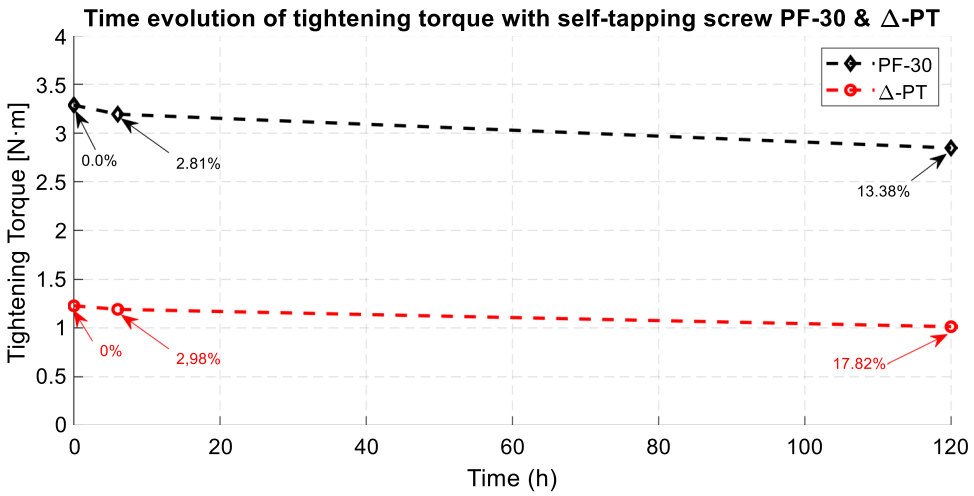

Fig. 14 Time evolution of tightening torque using PF-30 and Δ-PT

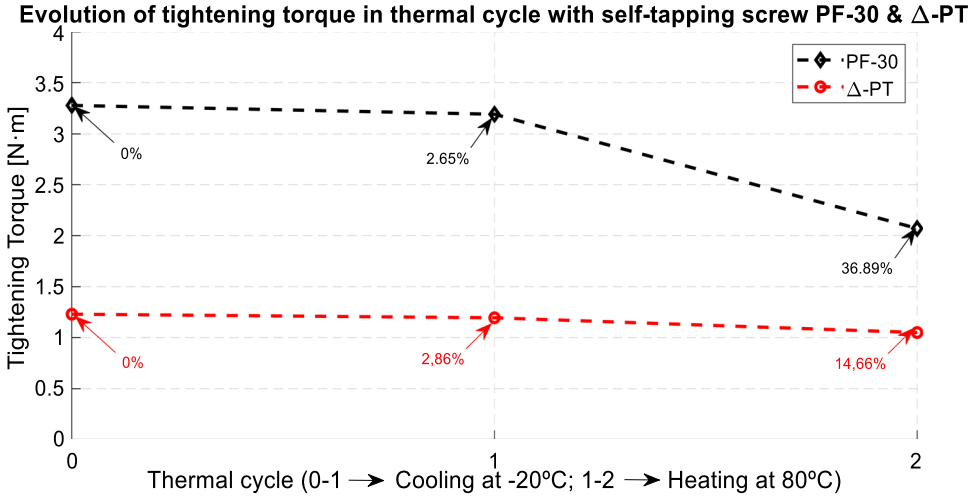

Fig. 15 Evolution of tightening torque in thermal cycle using PF-30 and Δ-PT

The tests were carried out using the same boss hole diameter and the same bolting length. The procedure is as follows:

1. Using a single boss for each screw in each repeat assembly, a screwdriving speed is set and the angles rotated are limited to a known tightening torque. For this test, the tightening torque was limited to 2/3 of the T_s-T_i straight line and with the screw configuration of 24 mm in length.
2. In each assembly, the loosening torque is determined when the joint is released.

The results shown in Fig. 13 show that the first disassembly, when carried out immediately after tightening, the losses can be considered negligible. However, in successive disassemblies, there are notable differences. In the case of the PF-30 screw, in the third assembly, the maximum loss of tightening torque occurs, reaching 11.95%, after which it decreases more slowly until the fifth assembly, where it loses 15.31%; after the fifth assembly, the trend of loss is very smooth, reaching 17.16% in the tenth assembly. In the case of the Δ-PT screw, the most significant loss of tightening torque occurs in the fifth assembly, 56.73%, after which it recovers slightly and remains practically constant, in the tenth assembly a loss of 41.93% occurs.

4.4 Evaluation of tightening loss over time

The objective of these tests seeks to determine the loss of tightening of the assemblies over time. For these tests, the dimensions of the boss holes and the same length of the threaded screw are maintained. Three cases arise:

1. Instantaneous loosening, that is, unscrewing the assemblies immediately after assembling them at a certain tightening torque, in this case 1/2 of the T_s-T_i line has been established as the limit.
2. Loosen after 6 h.
3. Loosen after 120 h.

Figure 14 reveals that in both analysed screws there is a percentage trend in tightening loss; in the PF-30 case it has lost a tightening of 13.38% with respect to the initial tightening after 120 h, while the Δ-PT lost 17.82%.

4.5 Evaluation of the quality of the joint under thermal cycles

The objective of these tests seeks to determine the loss of tightening of the assemblies in the face of a thermal cycle. The tests are carried out with the same instructions as in the previous section.

Table 4 Summary results of numerical simulations vs experiments

	Numerical simulations results			Experimental results		
	t^* = 11 mm		t^* = 7 mm	t^* = 11 mm		t^* = 7 mm
	Ti (Nm)	Fv (kN)$\vert_{Tt=3.95\ Nm}$	Ti (Nm)	Ti (Nm)	Fv (kN)$\vert_{Tt=3.95\ Nm}$	Ti (Nm)
PF-30	1.80	2.15	2.18	1.78	2.18	1.98
	Ti (Nm)	Fv (kN)$\vert_{Tt=1.72\ Nm}$	Ti (Nm)	Ti (Nm)	Fv (kN)$\vert_{Tt=1.72\ Nm}$	Ti (Nm)
Δ-PT	1.32	0.90	1.58	1.30	0.91	1.44

*t = thickness plate

In view of the results shown in Fig. 15, cooling has little effect on the loss of tightening; it slightly recovers the relaxation effects produced over time. However, heating produces important effects on the assemblies. This is very noticeable in the case of the PF-30 screw, producing a loss of 36.89% after 2 h at 80 °C, while in the case of the Δ-PT screw, the loss is 14.66%.

Table 4 compares the main results obtained from the numerical simulations and the experimental results, and Table 5 summarizes the loss of tightening torque of the PF-30 and Δ-PT screws under repeatability, relaxation and the effect of thermal cycle.

Table 5 Loss of tightening torque

	Experimental results			
	Repeatability	*Relaxation*	*Thermal cycle*	
	% loss tightening torque at 10 assembly	% loss tightening torque at 120 h	% loss tightening torque at − 20 °C	% loss tightening torque at 80 °C
PF-30	17.16	13.38	2.65	36.89
Δ-PT	41.93	17.82	2.86	14.66

5 Conclusions

This study presents the joint of PEI polymer parts reinforced with fibre glass, which are increasingly being used in the automotive sector.

Modelling using the finite element method has been satisfactory, managing to reproduce the experimental results to a great extent. The TNV model chosen to model the PEI polymer turns out to be efficient and quite accurate, and the proposed methodology allows analysing any material and almost any geometry without the need to resort to a three-dimensional model that entails extremely high computational costs. The only limitation is the constitutive model of the polymer.

In addition, the bonding capacities of fibre glass reinforced PEI have been experimentally evaluated under conditions of repeatability, relaxation over time and thermal cycle using two geometries of self-tapping screws used in the automotive industry. In terms of repeatability, the PF-30 screw has been verified to lose 17.16% of the tightening torque in the tenth tightening; on the contrary, the Δ-PT screw loses up to 41.93%.

The loss of tightening over time is similar in both types of screws, with 13.38% and 17.82% for the PF-30 and Δ-PT screw, respectively.

Finally, in the thermal cycle, in the cooling stage the loss of tightening torque decreases slightly; however, when heated it has been verified that the PF-30 screw loses 36.89% of the tightening torque and the Δ-PT only loses 14.66%.

As future perspectives to continue expanding the knowledge of these processes, some lines are proposed that are indicated below in summary:

- Evaluate tightening conditions in vibration scenarios and under fluctuating stresses.
- Evaluate tightening conditions in combined scenarios.
- Evaluate joint failure mechanisms under different scenarios.
- Evaluate other polymeric materials with great perspective to replace metal parts in vehicle parts.
- Evaluate polymers with different percentages of fibre glass and how it affects working conditions, especially the repeatability of assembled parts.
- Develop numerical simulation models with complex and custom geometry.

Acknowledgements This paper has been written during the Margaritas Salas stay that links the corresponding author with the Polytechnical University of Cartagena, thanks to the requalification aid of the University System financed by the Ministry of Universities with Next Generation funds from the European Union.

Author contribution All authors contributed to the study conception and design. Material preparation, data collection and analysis were performed by Wilmer E. Cumbicus, Manuel Estrems, Miguel Arizmendi and Amaya Jiménez. The first draft of the manuscript was written by Wilmer E. Cumbicus and all authors commented on previous versions of the manuscript. All authors read and approved the final manuscript.

Funding Open Access funding provided thanks to the CRUE-CSIC agreement with Springer Nature.

Declarations

Competing interests The authors declare no competing interests.

References

1. Ohba T (2018) Polymeric materials for future automobiles. Int Polym Sci Technol 45:237–243. https://doi.org/10.1177/0307174X1804500511

2. Patil A, Patel A, Purohit R (2017) ScienceDirect An overview of polymeric materials for automotive applications. Mater Today Proc 4:3807–3815. https://doi.org/10.1016/j.matpr.2017.02.278
3. Sherrington DC (1998) Preparation, structure and morphology of polymer supports. Chem Commun 2275–2286. https://doi.org/10.1039/A803757D
4. Flory PJ (1945) Tensile strength in relation to molecular weight of high polymers. J Am Chem Soc 67:2048–2050. https://doi.org/10.1021/ja01227a506
5. Jeon J, Muliana A, La V (2014) Thermal stress and deformation analyses in fiber reinforced polymer composites undergoing heat conduction and mechanical loading. Compos Struct 111:31–44. https://doi.org/10.1016/j.compstruct.2013.11.027
6. Noriega R, Rivnay J, Vandewal K et al (2013) A general relationship between disorder, aggregation and charge transport in conjugated polymers. Nat Mater 12:1–7. https://doi.org/10.1038/nmat3722
7. Pandelidi C, Bateman S, Piegert S et al (2021) The technology of continuous fibre-reinforced polymers: a review on extrusion additive manufacturing methods. Int J Adv Manuf Technol 113:3057–3077. https://doi.org/10.1007/s00170-021-06837-6
8. Islam A, Hansen HN, Bondo M (2010) Experimental investigation of the factors influencing the polymer – polymer bond strength during two-component injection moulding. Int J Adv Manuf Technol 50:101–111. https://doi.org/10.1007/s00170-009-2507-8
9. Landesmann A, Seruti CA, Batista EDM et al (2015) Mechanical properties of glass fiber reinforced polymers members for structural applications. Mater Res 18:1372–1383. https://doi.org/10.1590/1516-1439.044615
10. Liu T, Lee J, Liu G, Wu Z (2013) Monitoring and diagnosis of the tapping process for product quality and automated manufacturing. Int J Adv Manuf Technol 64:1169–1175. https://doi.org/10.1007/s00170-012-4058-7
11. Chumakov R (2008) Optimal control of screwing speed in assembly with thread-forming screws. Int J Adv Manuf Technol 36:395–400. https://doi.org/10.1007/s00170-006-0839-1
12. Ehrenstein GW (2004) Handbuch Kunststoff-Verbindungstechnik. Hanser, München
13. Stéphan P, Mathurin F, Guillot J (2011) Analytical study of maximal tapping torque during forming screw process. J Mater Process Technol 211:212–221. https://doi.org/10.1016/j.jmatprotec.2010.09.013
14. Fukuoka T, Nomura M (2008) Proposition of helical thread modeling with accurate geometry and finite element analysis. J Press Vessel Technol Trans ASME 130:0112041–0112046. https://doi.org/10.1115/1.2826433
15. Mathurin F, Guillot J, Stéphan P, Daidié A (2009) 3D finite element modeling of an assembly process with thread forming screw. J Manuf Sci Eng Trans ASME 131:0410151–04101518. https://doi.org/10.1115/1.3160377
16 Jun H, Linbo ZHU, Baotong LI et al (2013) Three-dimensional finite element analysis of the mechanical properties. Chinese J Mech Eng 26:564–572. https://doi.org/10.3901/CJME.2013.03.564
17. Mackerle J (2003) Finite element analysis of fastening and joining: a bibliography (1990–2002). Int J Press Vessel Pip 80:253–271. https://doi.org/10.1016/S0308-0161(03)00030-9
18. Seneviratne LD, Ngemoh FA, Earles SWE (2000) An experimental investigation of torque signature signals for self-tapping screws. Proc Inst Mech Eng C J Mech Eng Sci 214:399–410. https://doi.org/10.1243/0954406001523065
19. Seneviratne LD, Ngemoh FA, Earles SWE, Althoefer KA (2001) Theoretical modelling of the self-tapping screw fastening process. Proc Inst Mech Eng, Part C: J Mech Eng Sci 215(2):135–154. https://doi.org/10.1243/0954406011520562
20. Ellwood KRJ, Fesko D, Bauer DR (2004) An axisymmetric model for thread forming in polycarbonate and polypropylene screw and boss fasteners. Polym Eng Sci 44:1498–1508. https://doi.org/10.1002/pen.20146
21. Cha J, Song HY, Hyun K, Go JS (2008) Rheological measurement of the nonlinear viscoelasticity of the ABS polymer and numerical simulation of thermoforming process radiative energy vacuum pressure. Int J Adv Manuf Technol 107:2449–2464. https://doi.org/10.1007/s00170-020-04979-7
22. Arruda E, Boyce M (1993) Evolution of plastic anisotropy in amorphous polymers during finite straining. Int J Plast 9(6):697–720. https://doi.org/10.1016/0749-6419(93)90034-N
23 Tomaš I, Cisilino AP, Frontini PM (2015) Una implementación implícita del modelo viscoplástico de Arruda-Boyce. Rev Int Metod Numer para Calc y Disen en Ing 31:171–181. https://doi.org/10.1016/j.rimni.2014.06.001
24. Arriaga A, Lazkano JM, Pagaldai R et al (2007) Finite-element analysis of quasi-static characterisation tests in thermoplastic materials: experimental and numerical analysis results correlation with ANSYS. Polym Test 26:284–305. https://doi.org/10.1016/j.polymertesting.2006.10.012
25. Bergstrom JS, Bischoff JE (2010) An advanced thermomechanical constitutive model for UHMWPE. Int J Struct Chang Solids 2:31–39
26. Sepiani H, Polak MA, Penlidis A (2020) Finite element implementation of viscoelastic and viscoplastic models. Eng Comput (Swansea, Wales) 37:2561–2585. https://doi.org/10.1108/EC-02-2019-0062
27. Cumbicus WE, Estrems M, Arizmendi M, Jiménez A (2021) Joining polymer parts with self-tapping screws: an improvement of the screw thread geometry. Int J Mater Form 14:777–798. https://doi.org/10.1007/s12289-020-01593-6
28. Abaqus (2017) ABAQUS 6.14 documentation. http://50.16.225.63/v2016/index.html. Accessed 14 Mar 2022
29. PolymerFEM (2021) MCalibration documentation. https://polymerfem.com/mcalibration/. Accessed 7 Jun 2021
30. Bergström JS (2015) Mechanics of solid polymers: theory and computational modeling. Elsevier, New York
31. Yeoh OH (1993) Some forms of the strain energy function for rubber. Rubber Chem Technol 66:754–771
32. Dratschmidt F, Ehrenstein GW (1997) Threaded joints in glass fiber reinforced polyamide. Polym Eng Sci 37:744–755. https://doi.org/10.1002/pen.11718